Alignment of Colloidal Rods in Crowded Environments

Macromolecules

pubs.acs.org/Macromolecules

Article

Alignment of Colloidal Rods in Crowded Environments

Vincenzo Calabrese,* Stylianos Varchanis, Simon J. Haward, and Amy Q. Shen*

Cite This: *Macromolecules* 2022, 55, 5610–5620

Read Online

ACCESS | Metrics & More | Article Recommendations | Supporting Information

ABSTRACT: Understanding the hydrodynamic alignment of colloidal rods in polymer solutions is pivotal for manufacturing structurally ordered materials. How polymer crowding influences the flow-induced alignment of suspended colloidal rods remains unclear when rods and polymers share similar length scales. We tackle this problem by analyzing the alignment of colloidal rods suspended in crowded polymer solutions and comparing that to the case where crowding is provided by additional colloidal rods in a pure solvent. We find that the polymer dynamics govern the onset of shear-induced alignment of colloidal rods suspended in polymer solutions, and the control parameter for the alignment of rods is the Weissenberg number, quantifying the elastic response of the polymer to an imposed flow. Moreover, we show that the increasing colloidal alignment with the shear rate follows a universal trend that is independent of the surrounding crowding environment. Our results indicate that colloidal rod alignment in polymer solutions can be predicted on the basis of the critical shear rate at which polymer coils are deformed by the flow, aiding the synthesis and design of anisotropic materials.

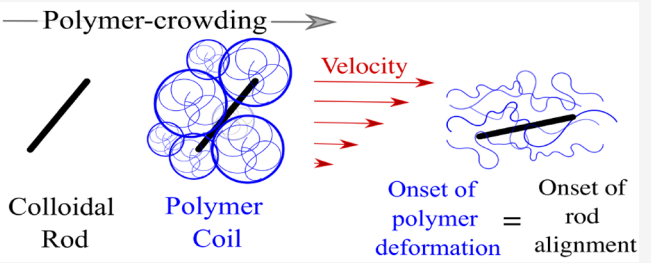

INTRODUCTION

The ability to control the hydrodynamic alignment of colloidal rods is critical to produce structurally ordered soft materials that possess desirable mechanical, thermal, optical, and electrical properties.[1−8] These anisotropic materials are promising in applications ranging from electronic sensors and soft robotics to tissue engineering and biomedical devices.[5,9−11] In materials science and engineering, colloidal rods are used in combination with other polymers that impart specific functionality to the final composite material (e.g., increasing ductility and mitigating embrittlement).[1,12,13] As such, understanding and controlling the hydrodynamic alignment of colloidal rods in polymer matrixes becomes of pivotal importance in large-scale processing operations.

The existing literature has shown that the most important control parameter for the onset of hydrodynamic alignment of rigid colloidal rods is the Péclet number $Pe = \dot{\gamma}/Dr$, a dimensionless number quantifying the relative strength between the imposed deformation rate (e.g., the shear rate ($\dot{\gamma}$) and the rotational diffusion coefficient of the rods (Dr)).[14−18] In dilute suspensions, the Péclet number can be defined as $Pe_0 = \dot{\gamma}/Dr_0$, with the rotational diffusion coefficient of the rods given as

$$Dr_0 = \frac{3k_bT\ln(l/d)}{\pi\eta_s l^3} \quad (1)$$

where d and l are the hydrodynamic diameter and length of the colloidal rod, respectively, $k_b = 1.38 \times 10^{-23}$ J/K is the Boltzmann constant, T is the absolute temperature, and η_s is the solvent viscosity. For $Pe_0 < 1$, Brownian flocculation dominates, whereas at $Pe_0 \geq 1$, convective forces are strong enough to induce alignment of the colloidal rods in the flow direction. However, this criterion is valid only under the assumption that the colloidal rods perceive the surrounding fluid as a continuum medium, that is, the characteristic length scale of the colloidal rods, such as the radius of gyration $Rg_r = \sqrt{\frac{d^2}{2} + \frac{l^2}{12}}$, must be much larger than that associated with the suspending medium.[19−21] Colloidal rods suspended in low M_w solvents such as water generally satisfy this assumption. However, in many industrial and biological processes, colloidal rods flow in crowded environments of polymers in solution where the characteristic length scale of suspended rods is similar to those of the surrounding macromolecules, for example, the polymer radius of gyration, Rg_p, or the polymer mesh size, ξ_p (also referred to as the correlation length).[20,22−27] In this scenario, the continuum assumption breaks down, and the rods experience a local viscosity (η_{local}) that lies between the solvent viscosity and the bulk viscosity of the polymeric solution.[22−24,27] In principle, with the knowledge of the value of η_{local}, it is possible to predict the shear rate

Received: April 14, 2022
Revised: May 31, 2022
Published: June 29, 2022

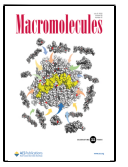

https://doi.org/10.1021/acs.macromol.2c00769
Macromolecules 2022, 55, 5610−5620

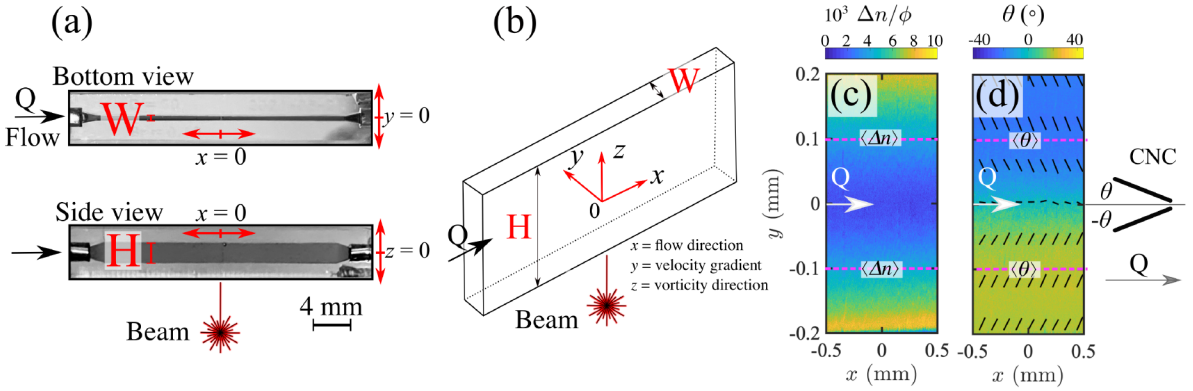

Figure 1. (a) Snapshots of the microfluidic platform from bottom and side views. (b) Schematic drawing with a coordinate system and relevant dimensions. (c, d) Time-averaged flow-induced birefringence (FIB) across the channel width for a representative test fluid composed of CNC at $\phi = 1 \times 10^{-3}$ suspended in water at an average velocity $U = 1.6 \times 10^{-3}$ m s^{-1}. In (c) the normalized birefringence intensity ($\Delta n/\phi$) and in (d) the orientation of the slow optical axis (θ), given by the contour plot (in full resolution) and depicted by the solid segments to guide the eye. The horizontal dashed lines in (c) and (d) indicate the location where the spatially averaged birefringence, $\langle \Delta n \rangle$, and the spatially averaged angle of slow axis, $\langle \theta \rangle$, are obtained for quantitative analysis.

for the onset of colloidal alignment based on the criterion of $Pe_0 = 1$ using η_{local} in place of η_s in eq 1. However, the main hurdle in predicting the alignment of colloidal rods suspended in macromolecular solutions based on the criterion $Pe_0 = 1$ stems from the fact that the value of η_{local} is not known *a priori*. Consequently, to date, it is challenging to predict the onset of flow-induced alignment of colloidal rods with length scales comparable to those of the suspending polymeric fluids.

The flow-induced alignment of rigid elongated particles suspended in viscoelastic polymeric solutions has been studied experimentally and numerically for particles with relevant length scales larger than that associated with the suspending fluid, thus, the suspending polymeric fluid was considered as a continuum medium for the colloidal rods.[26,28−32] In this length-scale context, theories predict a critical deformation rate above which the elastic forces of the suspending fluid cause the particle alignment to drift from the flow direction to the vorticity direction.[26,28,33,34] However, contrasting experimental results have been reported for relatively small particles suspended in shear-thinning polymeric fluids.[26,29,30] For instance, elongated hematite particles (with l = 600 nm) in entangled poly(ethylene oxide) solutions[30] displayed the particle alignment in the vorticity direction, as expected by theory. However, shorter hematite particles (with l = 360 nm) suspended in entangled polystyrene solutions[26] did not, casting doubts on the validity of continuum theories in conditions where colloids and polymers have similar characteristic length scales.

In this work, we elucidate the mechanism driving the onset of colloidal rod alignment in semidilute polymer solutions where polymers act as the crowding agents to tracer colloidal rods. We use cellulose nanocrystals (CNC) as rigid colloidal rods as they are widely used in the synthesis of composite polymer materials with high performance and functionalities.[13,35,36] To understand the effect of crowding on the CNC alignment, we adopt two approaches: (i) increasing the CNC mass fraction, ϕ, in an aqueous Newtonian solvent spanning from the dilute regime where interparticle interactions are negligible up to the semidilute regime where interparticle interactions are at play, providing "self-crowding" of the CNC by other analogous particles; (ii) using shear-thinning (non-Newtonian) polymer solutions as the suspending fluid while keeping $\phi = 1.0 \times 10^{-3}$ so that the CNC is in the dilute regime with negligible interparticle interactions, and the confinement acting on the CNC is provided only by the surrounding polymer chains, which we refer to as "polymer crowding". Specifically, we use high M_w neutral polymers (poly(ethylene oxide), PEO, and polyacrylamide, PA), with a radius of gyration Rg_p comparable to the CNC length scale (i.e., Rg_r).[23,37−40] For the polymer crowding case, we show that the onset of CNC alignment is linked with the relaxation time of the polymer solution (τ_p). Specifically, we show that the Weissenberg number $Wi = \tau_p\dot{\gamma}$, quantifying the strength of the elastic response of the fluid to an imposed deformation rate, controls the onset of CNC alignment in polymeric media.

EXPERIMENTAL SECTION

Test Fluids. The test fluids were prepared using an aqueous CNC stock suspension (CelluForce, Montreal, Canada, pH 6.3 at 5.6 wt %). The CNC has an average length $\langle l \rangle$ = 260 ± 180 nm, a maximum length l_{max} = 700 nm, an average diameter $\langle d \rangle$ = 4.8 ± 1.8 nm as detected from atomic force microscopy.[18] The CNC suspensions are electrostatically stabilized when suspended in deionized water with zero salt as a result of the presence of sulfate ester groups.[36,41] Therefore, the CNC bears a negative charge for a wide pH range, with a zeta potential of approximately −64 mV when suspended in deionized water at pH ≈7.[41] The effective hydrodynamic diameter is computed as $d = \delta + \langle d \rangle$ = 27.4 nm, considering the estimated contribution of the electric double layer δ = 22.6 nm in deionized water.[41] Assuming a cylindrical shape, the number density of the CNC was calculated as $\nu = (4\phi_{volume})/(\langle d \rangle^2 l\pi)$, where l is the hydrodynamic length of the CNC obtained experimentally through Dr_0 (specified in the main text) and ϕ_{volume} is the volume fraction of the suspended CNC (calculated using a CNC density of 1560 kg/m^3).[42] CNC suspensions at different mass fractions, ϕ, were prepared by dilution of the mother CNC stock with deionized water and mixed on a laboratory roller for at least 24 h at ∼22 °C. Where specified, the $\phi = 1 \times 10^{-3}$ CNC suspension was prepared in a Newtonian solvent composed of a glycerol/water mixture containing 17.2 vol % glycerol (Sigma-Aldrich 99% with η_s = 1.7 mPa s as measured via shear rheometry). From previous small-angle X-ray scattering studies of CNC suspensions from the same source as that used in the present work, we expect that, for $\phi < 5 \times 10^{-3}$, interparticle interactions are minimal.[43] From a geometrical argument, the rods are in the dilute regime for $\nu < 1/l^3$. Considering $\langle l \rangle$ = 260 ± 180 nm the

https://doi.org/10.1021/acs.macromol.2c00769
Macromolecules 2022, 55, 5610−5620

representative length, we expect the transition from dilute to semidilute to occur at $\phi \sim 2 \times 10^{-3}$.

PEO with $M_w \approx 4$ MDa, PEO with $M_w \approx 8$ MDa, and PA with $M_w \approx 5.5$ MDa, referred to as PEO4, PEO8, and PA5, respectively, were purchased from Sigma-Aldrich in powder form and solubilized in deionized water on a laboratory roller for at least 48 h at ∼22 °C (stock solution). Polymer solutions at different concentrations (c in mg/mL) containing a constant amount of CNC were prepared by diluting the polymer stock solution with deionized water followed by diluting the CNC stock suspension to a final $\phi = 1 \times 10^{-3}$ and then mixing the solution on a laboratory roller for 24 h at ∼22 °C. Polymer solutions without the CNC were prepared by following the same procedure described above. The polymer concentration where polymers begin to overlap was estimated as $c^* = M_w/((4\pi/3)Rg_p^3 N_A)$, where N_A is Avogadro's number.[38,44] The radius of gyration for the PEO4 and PEO8 was 135 and 202 nm, respectively, estimated as $Rg_p = 0.02M_w^{0.58}$.[37,38] For PA5, $Rg_p = (7.5 \times 10^{-3})M_w^{0.64} = 154$ nm.[39] For the PEO8, the polymer concentrations tested spanned between the dilute ($c/c^* < 1$) and semidilute unentangled regime, where $c/c^* > 1$ and the tube diameter $d_t = b_k\phi_p^{-0.75} > Rg_p$, where ϕ_p is the polymer volume fraction and $b_k \approx 3.7$ nm is the experimentally determined tube diameter in a PEO melt.[23,40,45] For PEO8 with $Rg_p = 202$ nm, the highest polymer concentration tested is $c/c^* = 10.5$, which yields $d_t \approx 250$ nm, thus in the semidilute unentangled regime ($c/c^* > 1$ and $d_t > Rg_p$). The ratio between the average CNC length and the PEO persistence length ($l_p \approx 0.5$ nm)[46] is $\langle l \rangle / l_p \sim 500$. The PEO is considered a compatible, nonadsorbing polymer for the CNC.[13,47] In the range of CNC and polymer concentrations tested, the CNC did not show any sign of aggregation, even after a few months from the sample preparation.

Methods. To assess the CNC alignment in crowded environments, we measured the flow-induced birefringence (FIB) as a function of the shear rate in a straight microfluidic channel etched in fused silica (Figure 1a,b). The microfluidic channel has a rectangular cross section with height $H = 2$ mm along the z-axis, corresponding to the optical path, and width $W = 0.4$ mm, along the y-axis, thus providing an approximation to two-dimension (2D).[18,48] The flow in the microfluidic channel is driven along the channel length (x-axis) by a syringe pump (Cetoni Nemesys) and Hamilton Gastight syringes infusing and withdrawing at an equal and opposite volumetric flow rate (Q) from the inlet and outlet, respectively. The average flow velocity in the channel is $U = Q(WH)^{-1}$.

Flow-Induced Birefringence (FIB). Time-averaged FIB measurements were performed using an Exicor MicroImager (Hinds Instruments, Inc., OR) using a 5× objective at room temperature (∼22 °C). The channel is illuminated through the z-axis (vorticity direction) using a monochromatic beam of wavelength $\lambda = 450$ nm or $\lambda = 630$ nm (see Figure 1a,b). The retardance, R in nm, and the orientation of the slow optical axis (extraordinary ray), θ, were obtained from seven images acquired at 1 s intervals and time-averaged. The spatially resolved (spatial resolution of Δn and θ is ≈2 μm/pixel) and time-averaged birefringence ($\Delta n = R/H$) and the orientation of the slow optical axis, θ, are obtained in the flow-velocity gradient plane ($x-y$ plane), as shown in Figure 1c,d, respectively, for a representative test fluid of dilute CNC in water. For CNC, θ probes the angle between the main CNC axis and the flow direction projected in the flow-velocity gradient plane. We note that the birefringence originates from the collective alignment of all the CNC rods present through the optical path (z-axis). At $\phi = 1 \times 10^{-3}$ we estimate that a total of $\approx 1 \times 10^6$ rods/pixel are probed simultaneously in the FIB experiment (see Supporting Information). As multiple rods are probed over a relatively long time frame (7 s), our FIB setup provides insights regarding the most favorable orientation of CNC under flow but not on the detailed orientation statistics such as the CNC orientation distribution. For this reason, we note that occasional tumbling of a small population of the CNC cannot be identified. For each flow rate, the birefringence Δn and the absolute value of the orientation of the slow optical axis, $|\theta|$, are spatially averaged along 1 mm of the x-axis at $y = \pm 0.1$ mm (see dashed lines in Figure 1c,d) and referred to as $\langle \Delta n \rangle$ and $\langle \theta \rangle$, respectively. The background value of Δn acquired at rest was subtracted for all the analyses presented, and quantitative analysis of θ is restricted to $\Delta n > 3 \times 10^{-6}$. The orientation angle $\langle \theta \rangle$ probes the CNC orientation with respect to the flow direction, whereas the birefringence intensity, $\langle \Delta n \rangle$, probes the extent of anisotropy in the system. For fully isotropically oriented particles, $\langle \Delta n \rangle = 0$ with colloidal alignment occurring for $\langle \theta \rangle < 45°$ and $\langle \Delta n \rangle > 0$.[49,50] The error related to the spatially averaged $\langle \Delta n \rangle$ and $\langle \theta \rangle$ is the standard deviation from the averaging process.

Rheology and Flow Simulations. Shear rheometry of the test fluids was performed using a strain-controlled ARES-G2 rotational rheometer (TA Instrument Inc.) equipped with a stainless steel cone and plate geometry (50 mm diameter and 1° cone angle). The test fluids were covered with a solvent trap and measured at 25 ± 0.1 °C (controlled by an advanced Peltier system, TA Instruments). The viscosity of the tested fluids was measured in "steady-state sensing" mode as a function of the shear rate ($\dot{\gamma}$). The rheometer determines automatically when the measurement reaches a steady state before moving to the next shear rate. For all fluids, the measured viscosity was independent of the preshear protocol with no hysteresis observed during either increasing or decreasing shear rate ramps, indicating negligible thixotropic effects. The data acquired below a torque limit of 0.5 μN m were discarded. The shear viscosity data were fitted to the Carreau−Yasuda (CY) generalized Newtonian model:

$$\eta = \eta_\infty + \frac{\eta_0 - \eta_\infty}{[1 + (\dot{\gamma}/\dot{\gamma}^*)^a]^{(1-n)/a}} \tag{2}$$

where η_0 is the zero-shear-rate viscosity, η_∞ is the infinite shear-rate viscosity, $\dot{\gamma}^*$ is the characteristic shear rate for the onset of shear thinning, n is the power law exponent, and a is a dimensionless fitting parameter that controls the transition to the shear-thinning region. The velocity field along the channel width (W, y-axis) and the value of the shear rate at $y = |0.1|$ mm (the channel location where $\langle \Delta n \rangle$ and $\langle \theta \rangle$ are obtained) were computed using numerical simulations. In the simulations, we consider the idealized problem in which an incompressible generalized Newtonian fluid with constant density ρ flows between two parallel infinite plates at a uniform temperature. The distance between the plates is W. The problem is to determine the velocity field together with the stress field. The velocity of the fluid is assumed to vary only in the y-direction; entrance and exit effects, as well as the presence of side walls, are neglected. Gravitational phenomena are not taken into consideration. Moreover, steady state is assumed and all time derivatives are neglected. The simplified equation of motion can be written as

$$-\frac{\partial P}{\partial x} + \frac{\partial \tau_{xy}}{\partial y} = 0 \tag{3}$$

where P is the thermodynamic pressure and τ_{xy} is the shear stress. According to the CY model,

$$\tau_{xy} = \left(\eta_\infty + \frac{\eta_0 - \eta_\infty}{\left[1 + \left(\left| \frac{\partial u_x}{\partial y} \right| / \dot{\gamma}^* \right)^a \right]^{(1-n)/a}} \right) \frac{\partial u_x}{\partial y} \tag{4}$$

Finally, the pressure gradient, $\partial P/\partial x$, is calculated by imposing a specified mean velocity across the channel:

$$\int_{-W/2}^{W/2} u_x \, dy = \frac{Q}{WH} \tag{5}$$

The aforementioned system of equations is discretized and solved using an in-house Finite Element solver.[51] In all simulations, 200 linear elements were used across the width of the channel. For each average velocity used during the FIB experiment, $\langle \Delta n \rangle$ and $\langle \theta \rangle$ are

https://doi.org/10.1021/acs.macromol.2c00769
Macromolecules 2022, 55, 5610−5620

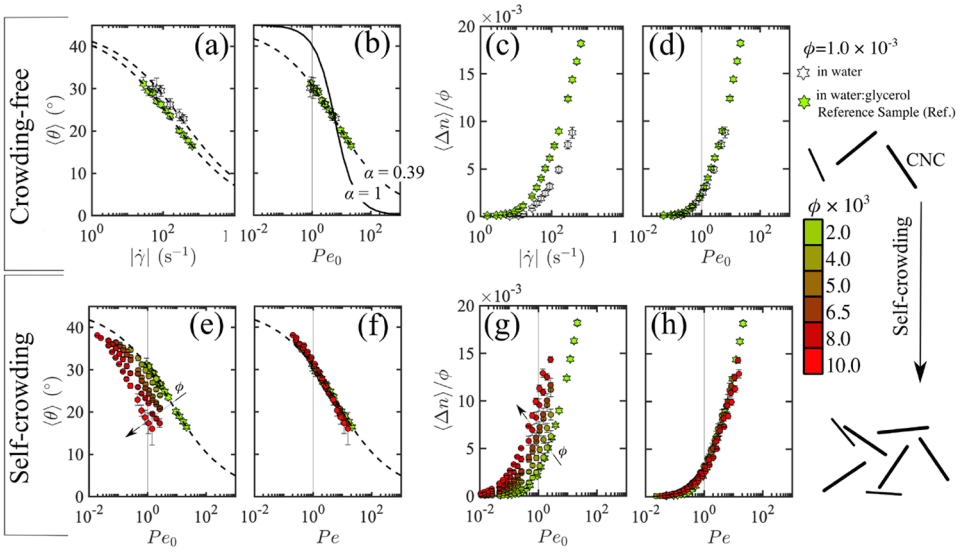

Figure 2. Spatially averaged orientation angle $\langle\theta\rangle$ (a, b, e, f) and normalized birefringence $\langle\Delta n\rangle/\phi$ (c, d, g, h) for CNC suspensions in the crowding-free (a–d) and self-crowding (e–h) regime. Open and green-filled stars represent CNC in water and in a water/glycerol mixture (17.2 vol % glycerol), respectively (crowding-free). For the samples prepared in water, the CNC rotational diffusion coefficient in the crowding-free regime is $Dr_0 = 59\ s^{-1}$, whereas $Dr_0 = 31\ s^{-1}$ for the sample prepared in the water/glycerol mixture labeled by the green star symbol and used as a reference sample (Ref.). For the crowding-free regime, $\langle\theta\rangle$ (a) and $\langle\Delta n\rangle/\phi$ (c) as a function of $|\dot{\gamma}|$ and scaled as $Pe_0 = |\dot{\gamma}|/Dr_0$ in (b) and (d), respectively. For the self-crowding regime, $\langle\theta\rangle$ (e) and $\langle\Delta n\rangle/\phi$ (g) as a function of Pe_0 and scaled as $Pe = |\dot{\gamma}|/Dr$ in (f) and (h), respectively. The dashed lines in (a, b, e, f) are the fittings to eq 6 with $\alpha = 0.39$. In (b) eq 6 is also plotted using $\alpha = 1$ (solid line). Vertical lines at $Pe_0 = 1$ and $Pe = 1$ are drawn as a reference. Error bars indicate the standard deviation of the measurement.

compared with the effective value of $|\dot{\gamma}|$ obtained from the simulation at $y = |0.1|$ mm. The channel location of $y = \pm 0.1$ mm is chosen to be the midpoint between the side walls ($y = \pm 0.2$ mm) and the centerline ($y = 0$ mm) to provide relatively high values of shear rate while avoiding undesired wall effects in the FIB experiment. For very weak shear-thinning fluids, for which the CY model could not be fitted to the rheological data, the shear rate was computed like that for a Newtonian fluid.

RESULTS AND DISCUSSION

Crowding-Free. We begin with the evaluation of the FIB of dilute CNC at $\phi = 1.0 \times 10^{-3}$ suspended in aqueous Newtonian media, either in water ($\eta_s = 0.9$ mPa·s) or a water/glycerol mixture (17.2 vol % glycerol, $\eta_s = 1.7$ mPa·s), shown in Figure 2a–d. At this relatively low CNC concentration, interparticle interactions are negligible so that each CNC can be considered as isolated and crowding-free.[43] Figure 2a,c present the $\langle\theta\rangle$ and $\langle\Delta n\rangle/\phi$ as a function of $|\dot{\gamma}|$ for the CNC in the crowding-free regime, respectively. For both media, the orientation angle, $\langle\theta\rangle$, displays a gradual decrease with $|\dot{\gamma}|$ (Figure 2a), and for a given value of $|\dot{\gamma}|$, the greater solvent viscosity of the water/glycerol mixture favors the CNC to align with a smaller value of $\langle\theta\rangle$ compared to that for water as the solvent. Moreover, the greater viscosity of the water/glycerol media triggers the onset of CNC alignment at a lower shear rate than that in water, as indicated by the onset of birefringence occurring at lower values of $|\dot{\gamma}|$ (Figure 2c).

The effective rotational diffusion coefficient Dr of the CNC is obtained experimentally based on

$$\langle\theta\rangle = \frac{\pi}{4} - \frac{1}{2}\arctan\left[\left(\frac{|\dot{\gamma}|}{6Dr}\right)^{\alpha}\right] \quad (6)$$

where $0 < \alpha \leq 1$ is a stretching exponent that accounts for particle polydispersity.[50,52−54] For monodisperse particles, $\alpha = 1$, whereas for polydisperse particles $\alpha < 1$ (see solid and dashed lines in Figure 2b). Fitting the data in Figure 2a with eq 6 yields $\alpha = 0.39$ for both Newtonian solvents, whereas $Dr_0 = 59\ s^{-1}$ and $Dr_0 = 31\ s^{-1}$ for the water and water/glycerol solvents, respectively. The subscript "0" to Dr indicates the crowding-free regime (i.e., dilute CNC in a continuum medium) and is used to distinguish it from the case where Dr is affected by the surrounding crowding agent. By solving eq 1 for l and using an effective CNC diameter $d = 27.4$ nm by accounting for the contribution from the electric double layer[41] and $T = 22$ °C, we obtain $l = 610$ nm, in accordance with the longest CNC population detected via microscopy in our previous work.[18] Our experimental data collapse onto master curves when we plot $\langle\theta\rangle$ and $\langle\Delta n\rangle/\phi$ as a function of the respective Péclet number in the crowding-free regime, $Pe_0 = |\dot{\gamma}|/Dr_0$, and the birefringence signal increases sharply at $Pe_0 = 1$, indicating that the Pe_0 scaling is correct (Figure 2b,d). It is expected that the Pe_0 scaling yields master plots of $\langle\theta\rangle$ and $\langle\Delta n\rangle/\phi$ only for the systems where the CNC is not experiencing any confinement. It is important to note that $\langle\Delta n\rangle$ and $\langle\theta\rangle$ are complementary parameters to quantify particle alignment during flow. The magnitude of birefringence $\langle\Delta n\rangle$ is linearly related to the number of aligned particles in a given illuminated volume, thus presented in a normalized form as $\langle\Delta n\rangle/\phi$. Contrarily, for a uniform particle alignment, $\langle\theta\rangle$ captures a geometrical property of the system that is independent from the number of aligned particles in a given illuminated volume.[49] With our experimental setup, we are unable to probe occasional tumbling of the CNC. However, because of the relatively high aspect ratio of the CNC ($\langle l\rangle/\langle d\rangle \approx 55$), we expect that deterministic tumbling does not occur within our experimental Pe_0 range ($0.01 < Pe_0 < 300$) and that the CNCs are mostly aligned in the flow direction at

https://doi.org/10.1021/acs.macromol.2c00769
Macromolecules 2022, 55, 5610−5620

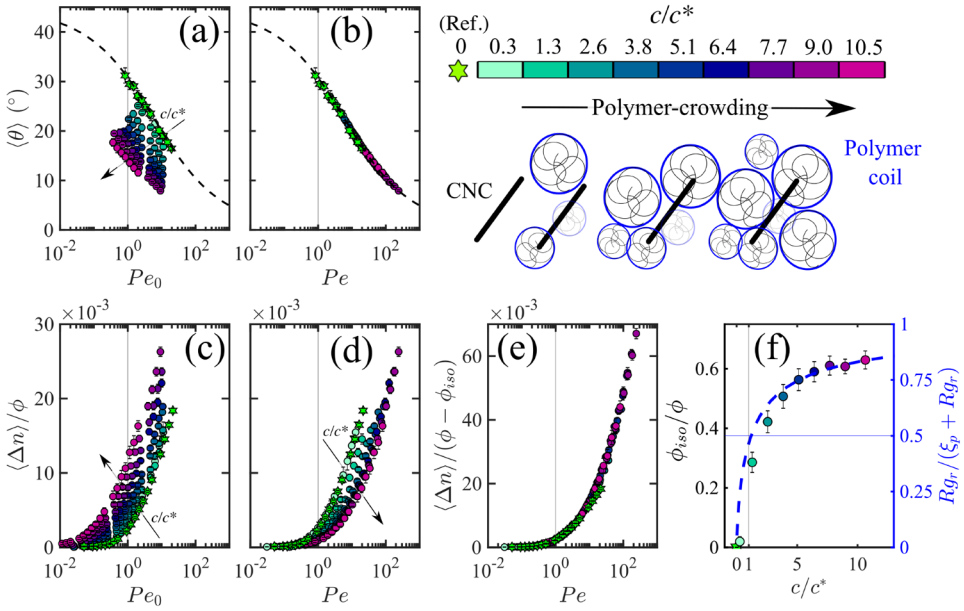

Figure 3. Spatially averaged birefringence $\langle \Delta n \rangle$ and orientation angle $\langle \theta \rangle$ for PEO8 solutions, at different c/c^*, seeded with CNC at $\phi = 1.0 \times 10^{-3}$. The PEO8 solutions are prepared in water; thus, the rotational diffusion coefficient in the crowding-free regime is $Dr_0 = 59\ s^{-1}$, whereas $Dr_0 = 31\ s^{-1}$ for the reference water/glycerol mixture, labeled by the green star symbol (Ref.). Orientation angle $\langle \theta \rangle$ (a) and normalized birefringence $\langle \Delta n \rangle/\phi$ (c) as a function of $Pe_0 = |\dot{\gamma}|/Dr_0$ and scaled as $Pe = |\dot{\gamma}|/Dr$ in (b) and (d), respectively. In (e) the birefringence $\langle \Delta n \rangle$ is scaled as $\langle \Delta n \rangle/(\phi - \phi_{iso})$ where $\phi - \phi_{iso} = \phi_{eff}$ and plotted as a function of Pe. (f) The ϕ_{iso}/ϕ (circles) and $Rg_r/\left(\xi_p + Rg_r\right)$ (dashed blue line) as a function of polymer concentration (c/c^*). Rg_r is the radius of gyration of the CNC and ξ_p is the polymer mesh size (eq 7). The dashed line in (a) is an instance of the fittings to eq 6 with $\alpha = 0.39$. In (b) the curve described by eq 6 collapses onto a master curve. Vertical lines at $Pe_0 = 1$ and $Pe = 1$ are drawn as a reference. Error bars from panels (a)−(e) indicate the standard deviation of the measurement, whereas in (f) error bars indicate uncertainty associated with ϕ_{iso} calculation.

sufficiently high shear rates (details in the Supporting Information).[55]

Self-Crowding. Following the same approach as for the crowding-free case, we investigate the CNC alignment upon increasing CNC mass fraction ϕ so that analogous particles restrain the motion of each other, a regime that we refer to as self-crowding (Figure 2e,h). As a reference sample, we use the crowding-free suspension in water/glycerol mixture (see green star symbol). When the CNC concentration is increased, the values of $\langle \theta \rangle$ decrease with increasing ϕ (Figure 2e). Analogously, the birefringence onset occurs at smaller values of Pe_0, corresponding to lower values of $|\dot{\gamma}|$ (Figure 2g). This behavior can be explained by the restrained rotational motion of the CNC above the overlap concentration due to particle confinement, leading to a decreasing Dr with increasing ϕ. For each sample, Dr can be obtained by fitting the curves in Figure 2e with eq 6 using a fixed value of $\alpha = 0.39$, as established in the crowding-free regime. When $\langle \theta \rangle$ and $\langle \Delta n \rangle/\phi$ are plotted as a function of the Péclet number $Pe = |\dot{\gamma}|/Dr$, the curves collapse onto single master curves (Figure 2f,h) and eq 6 leads to the dashed line in Figure 2f. We note that, for $\langle \theta \rangle$, the master curve is set by considering only Pe as a scaling factor. Contrarily, for the birefringence $\langle \Delta n \rangle$, the CNC mass fraction ϕ needs to be considered; indeed, scaling the birefringence as $\langle \Delta n \rangle/\phi$ is required to collapse the curves onto a master curve.

Polymer Crowding. For the case of polymer crowding, we follow $\langle \theta \rangle$ and $\langle \Delta n \rangle$ arising from the alignment of diluted CNC ($\phi = 1.0 \times 10^{-3}$) in polymer solutions exposed to a shearing flow. We consider polymers with different M_w and concentrations to achieve viscoelastic polymer solutions with viscosity up to 400× the viscosity of water and relaxation times $0.04 < \tau_p < 0.7$ s to provide a large span of crowding environments to the CNC. We use aqueous solutions of poly(ethylene oxide) with $M_w \approx 4$ MDa and $M_w \approx 8$ MDa, referred to as PEO4 and PEO8, respectively, and polyacrylamide with $M_w \approx 5.5$ MDa, referred to as PA5. In the absence of CNC, these polymer solutions do not display any significant birefringence, ensuring that $\langle \Delta n \rangle$ and $\langle \theta \rangle$ signals measured for the CNC dispersions arise exclusively due to the CNC alignment. Here, we focus on PEO8 solutions; analysis for the PEO4 and PA5 solutions are given in the Supporting Information, Section 2. The confinement imposed on the CNC is tuned by the polymer concentration (c), expressed in normalized form as c/c^*, where c^* is the polymer overlap concentration (Figure 3). For the PEO8, $c^* = 0.39$ mg/mL. The PEO8 concentration in the polymer-crowded CNC dispersions is varied between the dilute regime, $c/c^* < 1$, and the semidilute unentangled regime, where $c/c^* > 1$ and the tube diameter (d_t) is greater than the PEO8 radius of gyration, $Rg_p = 202$ nm.[45] When the PEO8 concentration c/c^* is increased, the $\langle \theta \rangle$ decreases for a given shear rate; thus, $Pe_0 = |\dot{\gamma}|/Dr_0$ (see Figure 3a), and the onset of birefringence shifts toward lower values of Pe_0 (Figure 3c). Interestingly, when $\langle \theta \rangle$ is plotted as a function of $Pe = |\dot{\gamma}|/Dr$, using the values of Dr obtained from the fitting of eq 6, the curves collapse onto a master curve (Figure 3b), revealing that the alignment of the CNC occurs in a similar manner for different PEO8 concentrations. Elliptical hematite particles (with l = 600 nm and a cross section of 130 nm) in entangled PEO solutions have been reported to first orient along the flow direction and then evolve to orientations in the vorticity

https://doi.org/10.1021/acs.macromol.2c00769
Macromolecules 2022, 55, 5610−5620

direction.[30] However, within our experimental window, we could observe only $\langle \Delta n \rangle / \phi$ increasing as a function of Pe, without the birefringence drop associated with the particle alignment drifting from the flow direction to the vorticity direction.[26,29,30] Indeed, perfect alignment along the vorticity direction (z-axis) for particles with circular cross sections would lead to isotropic projections in the flow−velocity gradient plane ($x-y$ plane) with $\langle \Delta n \rangle = 0$. Similar to us, Johnson et al.[26] observed only the orientation in the flow direction for elliptical hematite particles (with l = 360 nm and a cross section of 100 nm) in entangled polystyrene solutions.

In contrast to the self-crowding cases, scaling $\langle \Delta n \rangle / \phi$ by Pe is insufficient to collapse the data onto a single master curve (Figure 3d). We re-analyze the data based on the hypothesis that the failure to collapse might be caused by a small population of CNCs which do not contribute to the $\langle \Delta n \rangle$ intensity by remaining within the PEO8 matrix. Indeed, scaling the $\langle \Delta n \rangle$ by an effective CNC mass fraction $\phi_{eff} = \phi - \phi_{iso}$ enables all the data to collapse onto a master curve (Figure 3e). For each c/c^*, ϕ_{eff} is obtained by minimizing the sum of squared residuals between the reference water/glycerol curve and the polymer-containing samples (detailed procedure is given in the Supporting Information, Section 3). The ϕ_{iso}/ϕ increases with c/c^*, and at $c/c^* \approx 5$, it seems to approach a plateau value $\phi_{iso}/\phi \approx 0.65$ (Figure 3f). It is instructive to understand the evolution of ϕ_{iso} from a topological perspective. We compare the radius of gyration of the CNC, $Rg_r = \sqrt{\frac{d^2}{2} + \frac{l^2}{12}}$ = 177 nm, using l = 610 nm as previously determined from Dr_0, and d = 27.4 nm, with a mesh size of the PEO8[38]

$$\xi_p = Rg_p (c/c^*)^{-0.75} \tag{7}$$

as a function of c/c^*, where Rg_p = 202 nm is the radius of gyration of PEO8. Specifically, we use the ratio $Rg_r/\left(\xi_p + Rg_r\right)$ to yield values between 0 ($\xi_p \to \infty$) and 1 ($\xi_p \to 0$). Both ϕ_{iso}/ϕ and the theoretical curve $Rg_r/\left(\xi_p + Rg_r\right)$, based on eq 7, display a similar trend as a function of c/c^*, suggesting that ϕ_{iso} is linked to the topological confinement exerted by the polymer mesh size ξ_p. Thus, at $c/c^* < 5$, ξ_p is a strong function of the polymer concentration, and ϕ_{iso}/ϕ increases likewise. Contrarily, at $c/c^* > 5$, ξ_p becomes a weaker function of c/c^*; accordingly, ϕ_{iso} starts to plateau. This suggests that the topological confinement exerted by the polymer mesh size ξ_p on the CNC leads to a population of trapped CNC within the PEO8 network that is unable to align in the flow direction at $Pe > 1$; thus, it remains in the isotropic state. Nonetheless, with our current FIB setup, it is impossible to provide a definitive evaluation by which a small population of CNC remains in an isotropic state (ϕ_{iso}) within the PEO8 matrix. Molecular dynamic simulation could provide insights into the nature of the mechanism that leads to a population of CNC that is not affected by the flow. Overall, our observations imply that the PEO8 provides a two-way topological hindrance to the CNC rotation, where a fraction of the CNC, ϕ_{eff}, perceives the confinement but is able to align at $Pe > 1$, whereas the other remaining fraction, ϕ_{iso}, is unable to align in the range of investigated Pe. Contrarily, for the case of self-crowding, all the CNC contribute to the birefringence signals, that is, $\phi = \phi_{eff}$. This significant difference between self-crowding and polymer crowding can be associated with the network formed from flexible PEO8 polymer chaining versus the network composed of rigid rodlike CNC. In the following sections, we examine the dependence of ϕ_{eff} on relevant length and time scales.

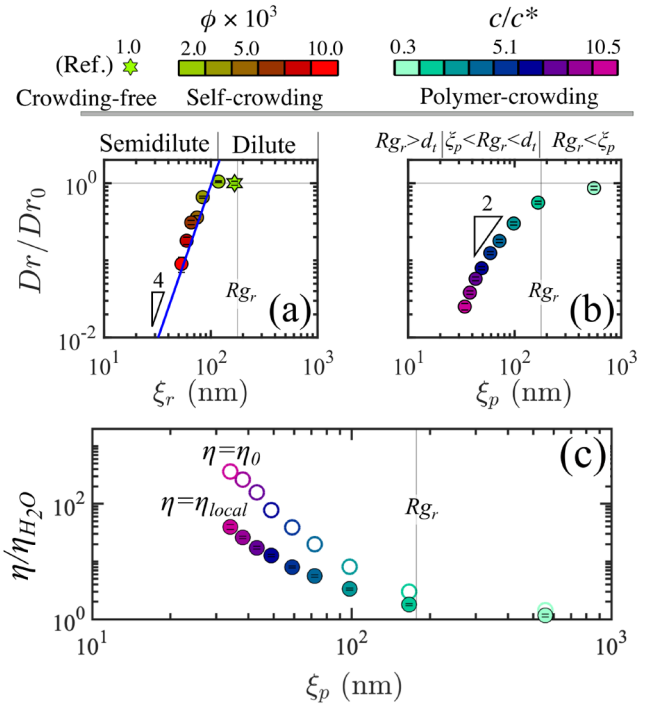

Figure 4. (a, b) Rotational diffusion coefficient of CNC, Dr, obtained from FIB (eq 6), normalized by the respective rotational diffusion coefficient in the crowding-free regime, Dr_0, as a function of the mesh size of the crowding agent ξ. (a) The case of self-crowding, given by an increasing CNC concentration with the corresponding mesh size ξ_r (eq 8). (b) The case of polymer crowding, given by an increasing PEO8 concentration with the corresponding mesh size ξ_p (eq 7). Relevant regimes for the (a) self-crowding and (b) polymer crowding are annexed above the respective panels. The line in (a) is the prediction from eq 10. In (b), the triangle indicates the scaling $Dr \propto \xi_r^2$ in the regime $\xi_p < Rg_r < d_t$. (c) Comparison between the normalized zero shear viscosity η_0/η_{H_2O} measured by bulk shear rheology (empty symbols), and the viscosity experienced by the CNC, η_{local}/η_{H_2O} (filled symbols), obtained by eq 11. Error bars in (a, b) indicate uncertainty associated with Dr obtained from the fitting procedure of eq 6.

Length-Scale Dependence. The rotational diffusion coefficient Dr obtained from eq 6 captures the impact of the crowding environment on the CNC. To compare the Dr for the case of self-crowding and polymer crowding, we plot Dr against the statistical mesh size ξ of each crowding agent. The mesh size of the polymer matrix is given by ξ_p (eq 7), whereas for the CNC suspension it is estimated as

$$\xi_r = (l\nu)^{-0.5} \tag{8}$$

where ν is the number density of the CNC (number of CNC per unit volume).[17,56] Importantly, as $\nu \propto l^{-1}$, ξ_r is independent from the rod length. For both cases, Dr decreases progressively with the decreasing ξ, indicating that the rods progressively sense the local confinement with the decreasing ξ_r or ξ_p. However, the CNC follows a much sharper decrease in Dr as a function of ξ for the case of self-crowding than that of the polymer crowding, indicating that the mesh size ξ alone is not

https://doi.org/10.1021/acs.macromol.2c00769
Macromolecules 2022, 55, 5610−5620

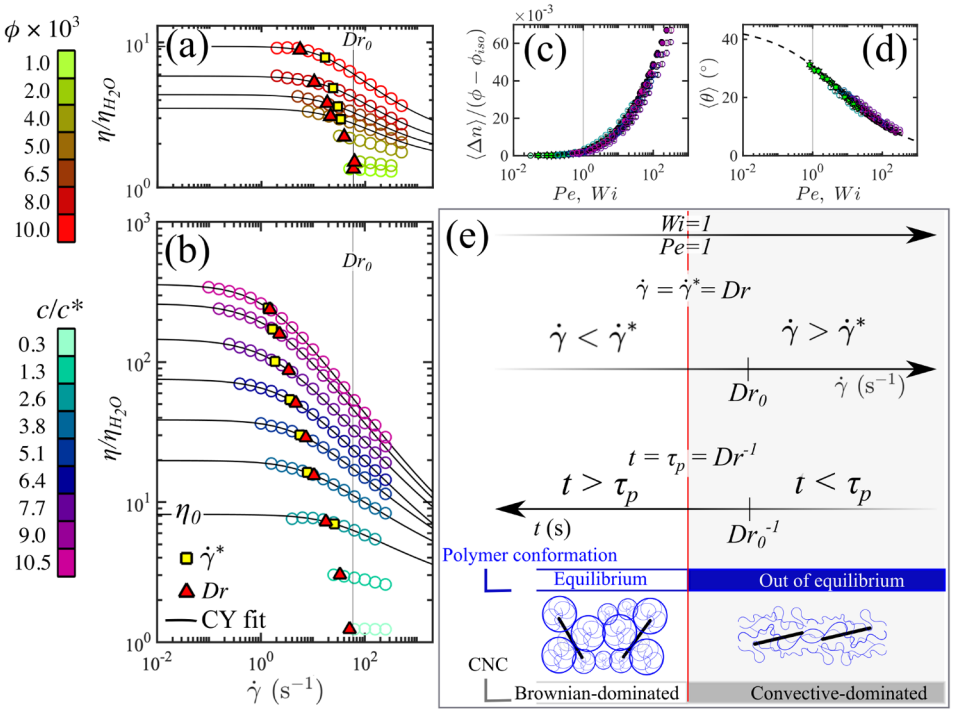

Figure 5. Steady shear viscosity measurements for (a) CNC suspended in water at different values of ϕ and (b) PEO8 solutions at different values of c/c^* (without CNC) presented as η/η_{H_2O} versus $\dot{\gamma}$. Solid lines in (a, b) describe the CY model (eq 2). The onset of shear thinning, $\dot{\gamma}^*$, obtained from the CY, and the value of *Dr* obtained from FIB measurements are plotted on the respective viscosity values. (c, d) Comparison between the *Pe* (filled symbols) and *Wi* (empty symbols) scaling for the normalized birefringence, $\langle\Delta n\rangle/(\phi-\phi_{iso})$, and orientation angle, $\langle\theta\rangle$, for the CNC in PEO8 solutions at different values of c/c^*. (e) Schematic of relevant time scales involved in the alignment of colloidal rods in polymer-crowding cases. The schematic is valid for polymers with relaxation time $\tau_p > Dr_0^{-1}$.

able to fully capture the dependence of *Dr* from the crowding agent. The *Dr* trend for the self-crowding case shown in Figure 4a meets the expectation from rigid-rod theory, where in the dilute regime *Dr* is concentration-independent and $Dr/Dr_0 = 1$. While in the semidilute (self-crowding) regime, the CNC motion is constrained by the surrounding rods and *Dr* becomes concentration-dependent.[14] The dependence of *Dr* with the rod concentration has been described by the tube model in the framework of the Doi–Edwards theory, assuming that particles are rigid and monodisperse rods in the semidilute regime, as

$$Dr/Dr_0 = \beta(\nu l^3)^{-2} \tag{9}$$

where β is a length-independent prefactor.[14,57,58] Recently, Lang et al.[17] experimentally validated for monodisperse colloidal rods that $\beta = 1.3 \times 10^3$, as previously found from computer simulation.[59] Rearranging eq 9 with eq 8, we obtain

$$Dr/Dr_0 = \beta\xi_r^{\,4} l^{-4} \tag{10}$$

Although polydisperisity is not accounted for in the Doi–Edwards theory, it is interesting to note that the $\xi_r^{\,4}$ scaling captures the Dr/Dr_0 trend for the self-crowding case (Figure 4a). Moreover, when $\beta = 1.3 \times 10^3$ and $l = 610$ nm are used in eq 10, it is possible to quantitatively capture the increasing Dr/Dr_0 with ξ_r in the semidilute (self-crowding) regime (see line in Figure 4a).

For the polymer-crowding case, we take inspiration from prior work on the translational and rotational diffusions of nanorods in PEO solutions.[20,22] Specifically, we adopt the scaling law by Cai et al.[20] developed for the translation diffusion coefficient of spherical particles in polymer solutions by considering Rg_r as the characteristic dimension of CNC. This choice is motivated by the work of Alam and Mukhopadhyay,[22] which found that the scaling law developed by Cai et al.[20] satisfactorily predicted the scaling of rotational and translation diffusion coefficients of nanorods in polyethylene glycol solutions as a function of the polymer concentration. The majority of our data fall in the "intermediate regime", where $\xi_p < Rg_r < d_t$, annotated above Figure 4b. In this regime, the scaling theory predicts $Dr \propto \xi_p^{\,2}$, which captures our trend reasonably well.[20] We have also used other polymeric solutions (PEO4 and PA5) to gain further understanding of the polymer-crowding cases. We confirm that the mesh size alone is unable to fully describe the dependence of *Dr* from the crowding agent; thus, the curves of Dr/Dr_0 versus ξ_p do not collapse onto a master curve (see Supporting Information, Figure S3). Because CNC in the PEO8 solutions is in the dilute regime ($\phi = 1.0 \times 10^{-3}$), it is instructive to evaluate the local viscosity experienced by the particles, η_{local}, as[23,24,60,61]

$$Dr/Dr_0 = \eta_{H_2O}/\eta_{local} \tag{11}$$

We use $Dr_0 = 59$ s^{-1} determined in water with η_{H_2O} being the water viscosity and *Dr* obtained experimentally from eq 6 (plotted in Figure 4a), to retrieve η_{local}. In Figure 4c, the zero shear-rate viscosity η_0 obtained from bulk rheology (details in Figure 5b) is compared to η_{local}, displaying $\eta_{local} < \eta_0$ in the investigated range of ξ_p. The mismatch between η_0 and η_{local}

https://doi.org/10.1021/acs.macromol.2c00769
Macromolecules 2022, 55, 5610–5620

indicates that the CNC does not perceive the surrounding medium as a continuum, thus experiencing a viscosity that lies between the water viscosity (η_{H_2O}) and the macroscopic bulk viscosity η_0 of the polymer solutions. Consequently, predicting the minimum shear rate required to induce CNC alignment in polymer crowds, based on the criterion $\dot{\gamma} = Dr$ (i.e., $Pe = 1$), using the bulk viscosity η_0 as the solvent viscosity in eq 1, would fail by underestimating Dr.

Time-Scale Dependence. Flow curves obtained from bulk shear rheometry were used to probe the two crowding agents, CNC suspensions in water and PEO8 solutions in the absence of CNC, under different shear rates and related flow time scales (i.e., $t = \dot{\gamma}^{-1}$); see Figure 5a,b. It is important to note that the presence of CNC at $\phi = 1.0 \times 10^{-3}$ in the PEO8 solutions did not alter the bulk rheology (see the Supporting Information, Figure S1). With increasing concentrations of the crowding agent (ϕ and c/c^* for the CNC and PEO8, respectively), the shear viscosity increases and the onset of shear thinning, captured by $\dot{\gamma}^*$ from the CY model (eq 2), shifts to lower values of shear rate (depicted by the yellow squares in Figure 5a,b). The Dr obtained via birefringence measurements (as shown in Figure 4a,b) are marked as triangular red symbols on the respective viscosity plots of the CNC suspensions and PEO8 solutions in Figure 5a,b.

For the CNC suspensions (Figure 5a), $\dot{\gamma}^*$ obtained from shear rheometry and Dr obtained via birefringence measurements have similar values because the onset of shear thinning correlates with the onset of CNC alignment. Therefore, the physical interpretation for the decreasing $\dot{\gamma}^*$ as a function of ϕ mirrors the one given for Dr. Specifically, in the semidilute (self-crowding) regime, the rods perceive the surrounding rods, enabling the onset of alignment at values of shear rate that decrease progressively with increasing ϕ. For the PEO8 solutions (Figure 5b), the onset of shear thinning, $\dot{\gamma}^*$, corresponds to the longest relaxation time of the polymer solution as $\tau_p = \dot{\gamma}^{*-1}$. In good approximation, the CNC alignment in PEO8 occurs at a shear rate $\dot{\gamma} = \dot{\gamma}^* = Dr$ (see yellow squares and red triangles in Figure 5b), suggesting that the onset of CNC alignment is coupled with the polymer relaxation time as $\tau_p = Dr^{-1}$. As such, a suitable control parameter for the CNC alignment is the Weissenberg number, $Wi = \tau_p\dot{\gamma}$, quantifying the strength of the elastic response of the fluid to an imposed deformation rate, where for $Wi < 1$ the polymers are in their equilibrium conformation but for $Wi \geq 1$ the relatively high flow rate drives the polymers out of their equilibrium conformation.[62−64] On the basis of the relationship $\tau_p = Dr^{-1}$, the Weissenberg and Péclet numbers become identical because the rotational diffusion time scale of the CNC rods is the same as the longest relaxation time of the polymer for the regime $\xi_p < Rg_r < d_t$ investigated here (analogous results are also obtained for the PEO4 and PA5 solutions presented in the Supporting Information, Figure S4). Consistently, the trend of CNC alignment in PEO8 solutions captured by $\langle\Delta n\rangle/\phi$ and $\langle\theta\rangle$ as a function of Pe is also well described by Wi, with the onset of CNC alignment occurring at $Pe = Wi = 1$ (Figure 5c,d). This is remarkably different from previous reports of elliptical hematite particles suspended in PEO solutions in the regime $Rg_r > d_t$, where the onset of alignment occurs at $Wi \ll 1$.[30] Similarly, the onset of alignment of carbon nanotubes in a sheared polymer melt was observed at $Wi \ll 1$, ruling out the coupling of τ_p with Dr for relatively large colloids ($Rg_r > d_t$).[29] From a topological perspective, the coupling between tracer particles and the polymer dynamics is predicted by Cai et al.[20] in the regime $\xi_p < Rg_r < d_t$ with the scaling $Dr \propto \xi_p^{\ 2}$ (see Figure 4b). It is possible to conceptualize the coupling of Dr with τ_p by analyzing three distinct time scales at play during flow as sketched in Figure 5e. For $t > \tau_p$, $(\dot{\gamma} < \dot{\gamma}^*)$, the polymer is relaxed and in its equilibrium configuration as the probed time scales are long enough to enable polymer relaxation, during which the CNC is able to escape from the transient confinement provided by the polymer mesh; thus, Brownian diffusion dominates. Increasing the shear rate, we reach $t = \tau_p$, $(\dot{\gamma} = \dot{\gamma}^*)$, where the polymer is driven out of its equilibrium conformation and deformed by the flow. At this time scale the CNC perceives the surrounding polymer as a static mesh that provides confinement and aids CNC alignment at values of $\dot{\gamma}^* = Dr$, $\left(\tau_p = Dr^{-1}\right)$. At higher values of shear rate, $t < \tau_p$, $(\dot{\gamma} > \dot{\gamma}^*)$, the CNC continues to align with the flow, following a universal curve of $\langle\theta\rangle$ and $\langle\Delta n\rangle/\phi_{eff}$ with respect to Pe for a wide range of polymer concentrations in the semidilute unentangled regime, as shown by the master curves in Figure 3b,e. We note that the CNC alignment for the polymer-crowding and self-crowding cases is analogous. In Figure 6 we plot together $\langle\theta\rangle$ and $\langle\Delta n\rangle/\phi_{eff}$ as obtained for all the polymer- and self-crowding cases presented above. The CNC alignment can be described by the same master curve of $\langle\theta\rangle$ and $\langle\Delta n\rangle/\phi_{eff}$ versus Pe. This observation implies that both self-crowding and polymer crowding of the CNC alters only the critical shear rate for the onset of alignment, but the subsequent trend in alignment for $Pe > 1$ remains the same for both cases. This universal trend with respect to the crowding agent is likely caused by the inability of the CNC to explore the surrounding confinement once the alignment is triggered by a sufficiently high shear rate (i.e., $Pe = 1$).[17] Note that in our present study the characteristic polymer time scale is greater than the rotational diffusion time scale of

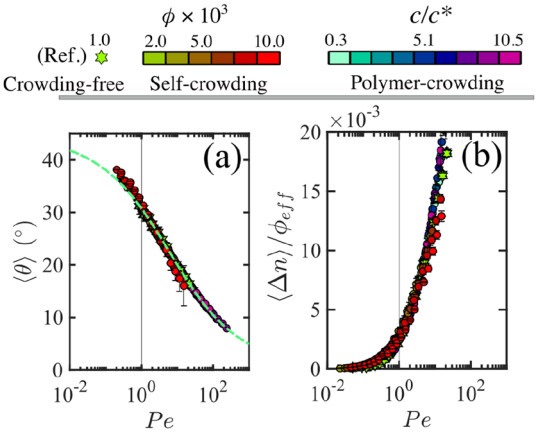

Figure 6. (a) Orientation angle, $\langle\theta\rangle$, and normalized birefringence, $\langle\Delta n\rangle/\phi_{eff}$, as a function of Pe for the self-crowding (from Figure 2f,h) and polymer crowding (from Figure 3b,e) for a total of 16 data sets including the reference sample. The dashed line in (a) is the plot of eq 6 using $\alpha = 0.39$.

https://doi.org/10.1021/acs.macromol.2c00769
Macromolecules 2022, 55, 5610−5620

the CNC in the crowding-free regime, $\tau_p > Dr_0^{-1}$, $(\dot{\gamma}^* < Dr_0)$; see the vertical line in Figure 5b with respect to $\dot{\gamma}^*$. However, colloidal rods with slower rotational dynamics in the crowding-free regime compared to those of the characteristic polymer time scale will be in the regime $\tau_p < Dr_0^{-1}$, $(\dot{\gamma}^* > Dr_0)$. Practically, this regime can be achieved by increasing the length of the colloidal rods ($Dr_0 \propto l^{-3}$) and/or decreasing the polymer molecular weight. As the regime $\tau_p < Dr_0^{-1}$ is approached, by for instance increasing l, the colloidal rods will progressively experience the surrounding environment as a continuum rather than a discrete medium and $\eta_{local} \rightarrow \eta_0$. Therefore, for $\tau_p \ll Dr_0^{-1}$, $(\dot{\gamma}^* \gg Dr_0)$, the onset of colloidal alignment is expected to be dominated by the bulk viscosity of the surrounding polymer solution.[19]

CONCLUSIONS

We tackle an industrially relevant problem from a fundamental perspective: the control over the alignment of rodlike colloids in polymeric matrixes. Specifically, we compare the flow-induced alignment of rigid colloidal rods, namely, CNC, in two contrasting crowded environments referred to as self-crowding and polymer crowding. By analysis of the length and time scales, we find that rotational diffusion coefficient, Dr, of CNC in high-molecular-weight polymeric crowds is coupled with the longest relaxation time of the surrounding polymer, τ_p. On this basis, we propose the Weissenberg number Wi as the control parameter for the alignment of colloidal rods that possess similar length scales as the suspending polymer fluid, $\xi_p < Rg_r < d_t$, that is, in conditions where the continuum approach breaks down. Specifically, we show that by knowing τ_p from rheological tests, it is possible to predict the critical shear rate for the onset of colloidal alignment in polymeric fluids as $\dot{\gamma} = \tau_p^{-1}$; equivalently, $Wi = 1$, without relying on the knowledge of the local viscosity experienced by the colloidal rods, η_{local}. In this work, we do not consider how the CNC dynamics are influenced by the polymer-depleted layer near the CNC surface because of the difficulty in estimating the depletion layer thickness for rodlike particles. We envisage that future work will be needed to understand the role of the depleted polymer layer, and its dynamic properties, on the CNC alignment under flow. In conclusion, our results provide crucial insights on the dynamics of colloidal rods under shearing flows that will aid the production of composite materials with desired structural organization. Additionally, the ability of tracer colloidal rods to probe the relaxation times of the surrounding polymers opens the opportunity to perform *in situ* and spatially resolved characterization of the dynamics of polymeric fluids under flow using tracer colloidal rods. With further optimization (e.g., size and composition of the colloidal rods), this technique is promising for analyzing polymer dynamics in complex flows encountered in real-life conditions where the investigation is a significant challenge. As a natural next step to our work, we envisage future studies where self-crowding and polymer crowding are at play jointly, mirroring actual industrial conditions. We use CNC as industrially relevant colloidal rods, but the basic principles will also apply to other anisotropic, rodlike, colloidal particles.

ASSOCIATED CONTENT

Supporting Information

The Supporting Information is available free of charge at https://pubs.acs.org/doi/10.1021/acs.macromol.2c00769.

Section 1, shear viscosity data for PEO8 with and without CNC and tabulated values from the fitting of the CY model (eq 2); section 2, experiments with additional polymer solutions (PEO4 and PA5); section 3, detailed procedure to estimate ϕ_{eff}; section 4, estimation of the probed number of rods in the FIB experiments; section 5, notes on deterministic tumbling for a dilute CNC suspension (PDF)

AUTHOR INFORMATION

Corresponding Authors

Vincenzo Calabrese − *Okinawa Institute of Science and Technology, Onna-son, Okinawa 904-0495, Japan;* orcid.org/0000-0001-5974-9217; Email: vincenzo.calabrese@oist.jp

Amy Q. Shen − *Okinawa Institute of Science and Technology, Onna-son, Okinawa 904-0495, Japan;* orcid.org/0000-0002-1222-6264; Email: amy.shen@oist.jp

Authors

Stylianos Varchanis − *Okinawa Institute of Science and Technology, Onna-son, Okinawa 904-0495, Japan*

Simon J. Haward − *Okinawa Institute of Science and Technology, Onna-son, Okinawa 904-0495, Japan;* orcid.org/0000-0002-1884-4100

Complete contact information is available at: https://pubs.acs.org/10.1021/acs.macromol.2c00769

Notes

The authors declare no competing financial interest.

ACKNOWLEDGMENTS

The authors gratefully acknowledge the support of Okinawa Institute of Science and Technology Graduate University with subsidy funding from the Cabinet Office, Government of Japan. V.C., S.V., S.J.H., and A.Q.S. also acknowledge financial support from the Japanese Society for the Promotion of Science (JSPS, Grant Nos. 22K14738, 22K14184, 18K03958, 18H01135, and 21K03884) and the Joint Research Projects (JRPs) supported by the JSPS and the Swiss National Science Foundation (SNSF).

REFERENCES

(1) Li, K.; et al. Alignment of Cellulose Nanofibers: Harnessing Nanoscale Properties to Macroscale Benefits. *ACS Nano* **2021**, *15*, 3646−3673.

(2) Mittal, N.; Ansari, F.; Gowda.V, K.; Brouzet, C.; Chen, P.; Larsson, P. T.; Roth, S. V.; Lundell, F.; Wågberg, L.; Kotov, N. A.; Söderberg, L. D. Multiscale Control of Nanocellulose Assembly: Transferring Remarkable Nanoscale Fibril Mechanics to Macroscale Fibers. *ACS Nano* **2018**, *12*, 6378−6388.

(3) Shen, Y.; Levin, A.; Kamada, A.; Toprakcioglu, Z.; Rodriguez-Garcia, M.; Xu, Y.; Knowles, T. P. From Protein Building Blocks to Functional Materials. *ACS Nano* **2021**, *15*, 5819−5837.

(4) Xin, G.; Zhu, W.; Deng, Y.; Cheng, J.; Zhang, L. T.; Chung, A. J.; De, S.; Lian, J. Microfluidics-enabled orientation and microstructure control of macroscopic graphene fibres. *Nat. Nanotechnol.* **2019**, *14*, 168−175.

(5) Sydney Gladman, A.; Matsumoto, E. A.; Nuzzo, R. G.; Mahadevan, L.; Lewis, J. A. Biomimetic 4D printing. *Nat. Mater.* **2016**, *15*, 413−418.
(6) Sano, K.; Ishida, Y.; Aida, T. Synthesis of Anisotropic Hydrogels and Their Applications. *Angewandte Chemie - International Edition* **2018**, *57*, 2532−2543.
(7) Peng, J.; Calabrese, V.; Veen, S. J.; Versluis, P.; Velikov, K. P.; Venema, P.; van der Linden, E. Rheology and microstructure of dispersions of protein fibrils and cellulose microfibrils. *Food Hydrocolloids* **2018**, *82*, 196−208.
(8) Håkansson, K. M. O.; Fall, A. B.; Lundell, F.; Yu, S.; Krywka, C.; Roth, S. V.; Santoro, G.; Kvick, M.; Prahl Wittberg, L.; Wågberg, L.; Söderberg, L. D. Hydrodynamic alignment and assembly of nanofibrils resulting in strong cellulose filaments. *Nat. Commun.* **2014**, *5*, 4018.
(9) Pei, X.; Zan, T.; Li, H.; Chen, Y.; Shi, L.; Zhang, Z. Pure Anisotropic Hydrogel with an Inherent Chiral Internal Structure Based on the Chiral Nematic Liquid Crystal Phase of Rodlike Viruses. *ACS Macro Lett.* **2015**, *4*, 1215−1219.
(10) Kiriya, D.; Kawano, R.; Onoe, H.; Takeuchi, S. Microfluidic control of the internal morphology in nanofiber-based macroscopic cables. *Angewandte Chemie - International Edition* **2012**, *51*, 7942−7947.
(11) De France, K. J.; Yager, K. G.; Chan, K. J. W.; Corbett, B.; Cranston, E. D.; Hoare, T. Injectable anisotropic nanocomposite hydrogels direct in situ growth and alignment of myotubes. *Nano Lett.* **2017**, *17*, 6487−6495.
(12) Kokkinis, D.; Schaffner, M.; Studart, A. R. Multimaterial magnetically assisted 3D printing of composite materials. *Nat. Commun.* **2015**, *6*, 8643.
(13) Wanasekara, N. D.; Eichhorn, S. J. Injectable Highly Loaded Cellulose Nanocrystal Fibers and Composites. *ACS Macro Lett.* **2017**, *6*, 1066−1070.
(14) Doi, M.; Edwards, S. F.; Edwards, S. F. *The Theory of Polymer Dynamics*; Oxford University Press: 1988.
(15) Lang, C.; Kohlbrecher, J.; Porcar, L.; Lettinga, M. The Connection between Biaxial Orientation and Shear Thinning for Quasi-Ideal Rods. *Polymers* **2016**, *8*, 291.
(16) Corona, P. T.; Ruocco, N.; Weigandt, K. M.; Leal, L. G.; Helgeson, M. E. Probing flow-induced nanostructure of complex fluids in arbitrary 2D flows using a fluidic four-roll mill (FFoRM). *Sci. Rep.* **2018**, *8*, 15559.
(17) Lang, C.; Kohlbrecher, J.; Porcar, L.; Radulescu, A.; Sellinghoff, K.; Dhont, J. K. G.; Lettinga, M. P. Microstructural understanding of the length- and stiffness-dependent shear thinning in semidilute colloidal rods. *Macromolecules* **2019**, *52*, 9604−9612.
(18) Calabrese, V.; Haward, S. J.; Shen, A. Q. Effects of Shearing and Extensional Flows on the Alignment of Colloidal Rods. *Macromolecules* **2021**, *54*, 4176−4185.
(19) Brochard Wyart, F.; de Gennes, P.G. Viscosity at small scales in polymer melts. *Eur. Phys. J. E* **2000**, *1*, 93−97.
(20) Cai, L. H.; Panyukov, S.; Rubinstein, M. Mobility of nonsticky nanoparticles in polymer liquids. *Macromolecules* **2011**, *44*, 7853−7863.
(21) Koenderink, G. H.; Zhang, H.; Aarts, D. G. A. L.; Lettinga, M. P.; Philipse, A. P.; Nägele, G. On the validity of Stokes−Einstein−Debye relations for rotational diffusion in colloidal suspensions. *Faraday Discuss.* **2003**, *123*, 335−354.
(22) Alam, S.; Mukhopadhyay, A. Translational and Rotational Diffusions of Nanorods within Semidilute and Entangled Polymer Solutions. *Macromolecules* **2014**, *47*, 6919−6924.
(23) Hess, M.; Gratz, M.; Remmer, H.; Webers, S.; Landers, J.; Borin, D.; Ludwig, F.; Wende, H.; Odenbach, S.; Tschöpe, A.; Schmidt, A. M. Scale-dependent particle diffusivity and apparent viscosity in polymer solutions as probed by dynamic magnetic nanorheology. *Soft Matter* **2020**, *16*, 7562−7575.
(24) Gratz, M.; Tschöpe, A. Size Effects in the Oscillatory Rotation Dynamics of Ni Nanorods in Poly(ethylene oxide) Solutions. *Macromolecules* **2019**, *52*, 6600−6612.
(25) Smith, M.; Poling-Skutvik, R.; Slim, A. H.; Willson, R. C.; Conrad, J. C. Dynamics of Flexible Viruses in Polymer Solutions. *Macromolecules* **2021**, *54*, 4557−4563.
(26) Johnson, S. J.; Salem, A. J.; Fuller, G. G. Dynamics of colloidal particles in sheared, non-Newtonian fluids. *J. Non-Newtonian Fluid Mech.* **1990**, *34*, 89−121.
(27) Lee, J.; Grein-Iankovski, A.; Narayanan, S.; Leheny, R. L. Nanorod mobility within entangled wormlike micelle solutions. *Macromolecules* **2017**, *50*, 406−415.
(28) Iso, Y.; Cohen, C.; Koch, D. L. Orientation in simple shear flow of semi-dilute fiber suspensions 2. Highly elastic fluids. *J. Non-Newtonian Fluid Mech.* **1996**, *62*, 135−153.
(29) Hobbie, E. K.; Wang, H.; Kim, H.; Lin-Gibson, S.; Grulke, E. A. Orientation of carbon nanotubes in a sheared polymer melt. *Phys. Fluids* **2003**, *15*, 1196−1202.
(30) Gunes, D.; Scirocco, R.; Mewis, J.; Vermant, J. Flow-induced orientation of non-spherical particles: Effect of aspect ratio and medium rheology. *J. Non-Newtonian Fluid Mech.* **2008**, *155*, 39−50.
(31) D'Avino, G.; Maffettone, P. Particle dynamics in viscoelastic liquids. *J. Non-Newtonian Fluid Mech.* **2015**, *215*, 80−104.
(32) D'Avino, G.; Hulsen, M. A.; Greco, F.; Maffettone, P. L. Numerical simulations on the dynamics of a spheroid in a viscoelastic liquid in a wide-slit microchannel. *J. Non-Newtonian Fluid Mech.* **2019**, *263*, 33−41.
(33) Leal, L. G. The slow motion of slender rod-like particles in a second-order fluid. *J. Fluid Mech.* **1975**, *69*, 305−337.
(34) Cohen, C.; Chung, B.; Stasiak, W. Orientation and rheology of rodlike particles with weak Brownian diffusion in a second-order fluid under simple shear flow. *Rheol. Acta* **1987**, *26*, 217−232.
(35) Hasegawa, H.; Horikawa, Y.; Shikata, T. Cellulose nanocrystals as a model substance for rigid rod particle suspension rheology. *Macromolecules* **2020**, *53*, 2677−2685.
(36) Eichhorn, S. J. Cellulose nanowhiskers: Promising materials for advanced applications. *Soft Matter* **2011**, *7*, 303−315.
(37) Devanand, K.; Selser, J. C. Asymptotic Behavior and Long-Range Interactions in Aqueous Solutions of Poly(ethylene oxide). *Macromolecules* **1991**, *24*, 5943−5947.
(38) Holyst, R.; Bielejewska, A.; Szymański, J.; Wilk, A.; Patkowski, A.; Gapiński, J.; Żywociński, A.; Kalwarczyk, T.; Kalwarczyk, E.; Tabaka, M.; Ziębacz, N.; Wieczorek, S. A. Scaling form of viscosity at all length-scales in poly(ethylene glycol) solutions studied by fluorescence correlation spectroscopy and capillary electrophoresis. *Phys. Chem. Chem. Phys.* **2009**, *11*, 9025.
(39) François, J.; Sarazin, D.; Schwartz, T.; Weill, G. Polyacrylamide in water: molecular weight dependence of $\langle R_2 \rangle$ and $[\eta]$ and the problem of the excluded volume exponent. *Polymer* **1979**, *20*, 969−975.
(40) Senses, E.; Faraone, A.; Akcora, P. Microscopic Chain Motion in Polymer Nanocomposites with Dynamically Asymmetric Interphases. *Sci. Rep.* **2016**, *6*, 29326.
(41) Bertsch, P.; Isabettini, S.; Fischer, P. Ion-induced hydrogel formation and nematic ordering of nanocrystalline cellulose suspensions. *Biomacromolecules* **2017**, *18*, 4060−4066.
(42) Wagner, R.; Raman, A.; Moon, R. Transverse Elasticity of Cellulose Nanocrystals via Atomic Force Microscopy. In *10th International Conference on Wood Biofiber Plastic Composites*, 2010; pp 309−316.
(43) Bertsch, P.; Sánchez-Ferrer, A.; Bagnani, M.; Isabettini, S.; Kohlbrecher, J.; Mezzenga, R.; Fischer, P. Ion-induced formation of nanocrystalline cellulose colloidal glasses containing nematic domains. *Langmuir* **2019**, *35*, 4117−4124.
(44) Ying, Q.; Chu, B. Overlap concentration of macromolecules in solution. *Macromolecules* **1987**, *20*, 362−366.
(45) Rubinstein, M.; Colby, R. H., et al. *Polymer physics*; Oxford University Press: New York, 2003; Vol. *23*.
(46) Dinic, J.; Sharma, V. Flexibility, extensibility, and ratio of Kuhn length to packing length govern the pinching dynamics, coil-stretch transition, and rheology of polymer solutions. *Macromolecules* **2020**, *53*, 4821−4835.

https://doi.org/10.1021/acs.macromol.2c00769
Macromolecules 2022, 55, 5610−5620

(47) Beuguel, Q.; Tavares, J. R.; Carreau, P. J.; Heuzey, M.-C. Rheological behavior of cellulose nanocrystal suspensions in polyethylene glycol. *J. Rheol.* **2018**, *62*, 607−618.
(48) Haward, S. J.; Toda-Peters, K.; Shen, A. Q. Steady viscoelastic flow around high-aspect-ratio, low-blockage-ratio microfluidic cylinders. *J. Non-Newtonian Fluid Mech.* **2018**, *254*, 23−35.
(49) Vermant, J.; Yang, H.; Fuller, G. G. Rheooptical determination of aspect ratio and polydispersity of nonspherical particles. *AIChE J.* **2001**, *47*, 790−798.
(50) Reddy, N. K.; Natale, G.; Prud'homme, R. K.; Vermant, J. Rheo-optical analysis of functionalized graphene suspensions. *Langmuir* **2018**, *34*, 7844−7851.
(51) Varchanis, S.; Syrakos, A.; Dimakopoulos, Y.; Tsamopoulos, J. A new finite element formulation for viscoelastic flows: Circumventing simultaneously the LBB condition and the high-Weissenberg number problem. *J. Non-Newtonian Fluid Mech.* **2019**, *267*, 78−97.
(52) Lindsey, C. P.; Patterson, G. D. Detailed comparison of the Williams-Watts and Cole-Davidson functions. *J. Chem. Phys.* **1980**, *73*, 3348−3357.
(53) Thurn, H.; Löbl, M.; Hoffmann, H. Viscoelastic detergent solutions. A quantitative comparison between theory and experiment. *J. Phys. Chem.* **1985**, *89*, 517−522.
(54) Decruppe, J. P.; Ponton, A. Flow birefringence, stress optical rule and rheology of four micellar solutions with the same low shear viscosity. *Eur. Phys. J. E* **2003**, *10*, 201−207.
(55) Zöttl, A.; Klop, K. E.; Balin, A. K.; Gao, Y.; Yeomans, J. M.; Aarts, D. G. Dynamics of individual Brownian rods in a microchannel flow. *Soft Matter* **2019**, *15*, 5810−5814.
(56) De Gennes, P.; Pincus, P.; Velasco, R.; Brochard, F. Remarks on polyelectrolyte conformation. *J. Phys. (Paris)* **1976**, *37*, 1461−1473.
(57) Doi, M.; Edwards, S. F. Dynamics of rod-like macromolecules in concentrated solution. Part 2. *J. Chem. Soc., Faraday Trans. 2* **1978**, *74*, 918−932.
(58) Doi, M.; Edwards, S. F. Dynamics of rod-like macromolecules in concentrated solution. Part 1. *J. Chem. Soc., Faraday Trans. 2* **1978**, *74*, 560−570.
(59) Teraoka, I.; Ookubo, N.; Hayakawa, R. Molecular theory on the entanglement effect of rodlike polymers. *Physical review letters* **1985**, *55*, 2712.
(60) Wisniewska, A.; Sozanski, K.; Kalwarczyk, T.; Kedra-Krolik, K.; Holyst, R. Scaling Equation for Viscosity of Polymer Mixtures in Solutions with Application to Diffusion of Molecular Probes. *Macromolecules* **2017**, *50*, 4555−4561.
(61) Choi, J.; Cargnello, M.; Murray, C. B.; Clarke, N.; Winey, K. I.; Composto, R. J. Fast Nanorod Diffusion through Entangled Polymer Melts. *ACS Macro Lett.* **2015**, *4*, 952−956.
(62) Nikoubashman, A.; Howard, M. P. Equilibrium Dynamics and Shear Rheology of Semiflexible Polymers in Solution. *Macromolecules* **2017**, *50*, 8279−8289.
(63) Ebagninin, K. W.; Benchabane, A.; Bekkour, K. Rheological characterization of poly(ethylene oxide) solutions of different molecular weights. *J. Colloid Interface Sci.* **2009**, *336*, 360−367.
(64) Dunderdale, G. J.; Davidson, S. J.; Ryan, A. J.; Mykhaylyk, O. O. Flow-induced crystallisation of polymers from aqueous solution. *Nat. Commun.* **2020**, *11*, 3372.

https://doi.org/10.1021/acs.macromol.2c00769
Macromolecules 2022, 55, 5610−5620